ACS OMEGA

Open Access

http://pubs.acs.org/journal/acsodf

Article

Self-Sanitization in a Silk Nanofibrous Network for Biodegradable $PM_{0.3}$ Filters with In Situ Joule Heating

Mozakkar Hossain,[#] Keshab Karmakar,[#] Prakash Sarkar, Tiyasi Chattaraj, and K. D. M. Rao*

Cite This: *ACS Omega* 2024, 9, 9137−9146

Read Online

ACCESS | Metrics & More | Article Recommendations | Supporting Information

ABSTRACT: In the contemporary way of life, face masks are crucial in managing disease transmission and battling air pollution. However, two key challenges, self-sanitization and biodegradation of face masks, need immediate attention, prompting the development of innovative solutions for the future. In this study, we present a novel approach that combines controlled acid hydrolysis and mechanical chopping to synthesize a silk nanofibrous network (SNN) seamlessly integrated with a wearable stainless steel mesh, resulting in the fabrication of self-sanitizable face masks. The distinct architecture of face masks showcases remarkable filtration efficiencies of 91.4, 95.4, and 98.3% for $PM_{0.3}$, $PM_{0.5}$, and $PM_{1.0}$, respectively, while maintaining a comfortable level of breathability (ΔP = 92 Pa). Additionally, the face mask shows that a remarkable thermal resistance of 472 °C cm^2 W^{-1} generates heat spontaneously at low voltage, deactivating *Escherichia coli* bacteria on the SNN, enabling self-sanitization. The SNN exhibited complete disintegration within the environment in just 10 days, highlighting the remarkable biodegradability of the face mask. The unique advantage of self-sanitization and biodegradation in a face mask filter is simultaneously achieved for the first time, which will open avenues to accomplish environmentally benign next-generation face masks.

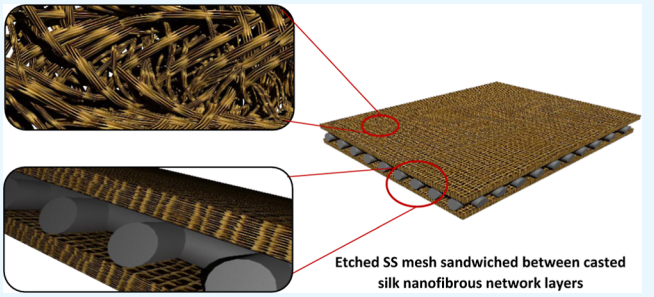

INTRODUCTION

In recent decades, rapid industrialization and urbanization have negatively impacted the natural atmosphere by increasing airborne particulate matter (PM) pollutants.[1−3] Specifically, PM smaller than 10 μm (PM_{10}) adversely affects human health.[4−7] Particles as small as 1.0 μm ($PM_{1.0}$) can be filtered using masks, but submicron $PM_{0.3}$ particles, which can carry pathogens, are the most concerning as they can penetrate the respiratory tract and bloodstream, leading to infectious diseases.[8,9] The global COVID-19 pandemic, caused by the SARS-COV-2 virus (∼120 nm in size), highlights the importance of aerosolized $PM_{0.3}$ in transmitting the virus.[10] The World Health Organization (WHO) recommended using face masks to curb the spread of the virus, making masks crucial for safeguarding against transmissible diseases and reducing air pollution.[11,12] Conventional face masks are typically made from fibrous polypropylene, but extended use can degrade their ability to capture pathogens and PM, which raises concerns about reusability.[13,14] Moreover, pathogens captured on mask surfaces remain active for days, posing a risk of secondary transmission.[15,16] Standard sanitization methods can harm mask filters and filtration efficiency (FE), making it crucial to sanitize masks effectively without compromising their ability to filter PM.[17] Face masks have become a fundamental aspect of everyday life because of the negative impact of airborne pollutants and the significant role of $PM_{0.3}$ in disease transmission.[12] Ensuring effective filtration and safe reusability of face masks, achieved through proper sanitization, is critical for combating disease transmission and mitigating air pollution.

Face masks are sanitized to eliminate pathogens using various methods such as dry heat, chemical reagents, nanoparticle implantation, and exposure to steam, supercritical CO_2, UV, and solar irradiation.[18−21] While dry heat and steam offer simple sanitization of face masks, the continuous temperature rise can lower filtration performance.[22] Conversely, UV and solar light irradiation effectively neutralize pathogens without compromising FE.[17,23] However, high-power UV requires specific chambers, and light irradiation may partially disinfect due to limited penetration.[24,25] Chemical sanitization involves agents like detergent, alcohol (IPA and ethanol), H_2O_2, hypochlorite, and ethylene oxide, ensuring thorough disinfection.[26] Nevertheless, these harsh chemicals disrupt mask filtration and leave harmful residues that distress the wearer's skin.[26] Addressing the need for on-the-spot mask sanitization, antibacterial nanoparticles (Cu, Ag, and TiO_2)

Received: October 13, 2023
Revised: January 23, 2024
Accepted: February 5, 2024
Published: February 15, 2024

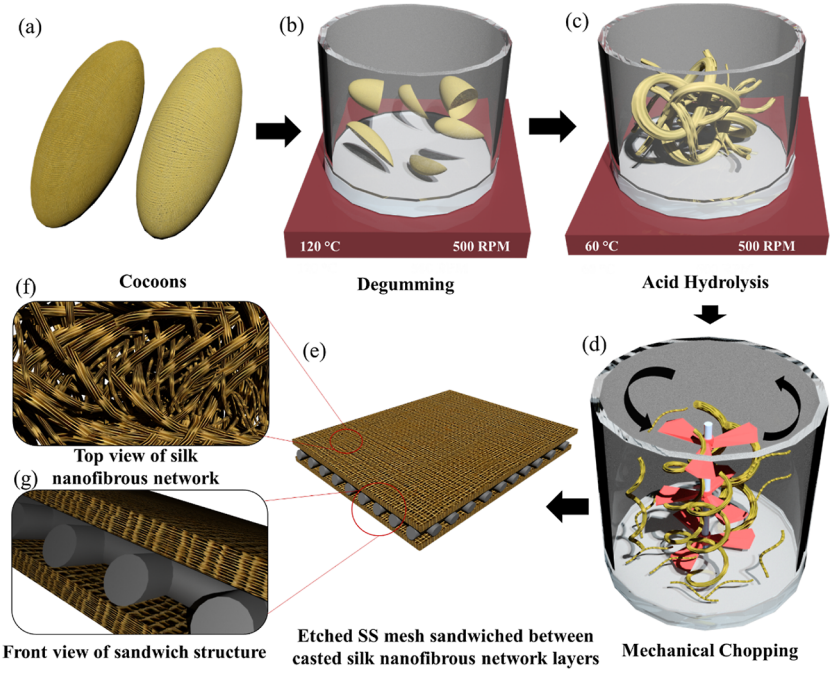

Figure 1. Schematic illustration of the synthesis of SNN for face masks. (a) Silkworm cocoons, (b) degumming process, (c) acid hydrolysis, and (d) mechanical chopping of silk fibers. (e) Self-sanitizable face mask fabricated by sandwiching the SS mesh in between the SNN layers; inset shows the magnified view of the (f) SNN and (g) SS mesh embedded with SNN.

have been implanted into masks, displaying significant antibacterial properties.[27,28] However, these nanoparticles have the potential to detach and be inhaled into the respiratory tract, posing potential health concerns.[29] Recent advancements include integrating one-dimensional nanowire networks into face masks for self-sanitization through photothermal and Joule-heating mechanisms.[30,31] The concept of self-sanitizing face masks is still being researched and developed. Thus, developing simple self-sanitization strategies is essential to disinfect face masks while maintaining an inherent filtration performance.

Commercial face masks typically utilize melt-blown nonwoven polypropylene (PP) and polystyrene (PS) fibers as filtration materials, hindering reusability and effective sanitization methods.[13,14] The alarming increase in single-use face mask disposal, reaching 129 billion in 2021 compared to 1.56 billion in 2020, emphasizes the need for environmentally friendly alternatives due to the nonbiodegradability of PP and PS fibers, contributing to plastic waste and microplastics in the ecosystem.[32,33] Efforts are made to find biodegradable filters for fabricating environmentally sustainable face masks. For instance, Le et al. introduced poly-L-lactic acid (PLLA) nanofibrous membranes, which exhibited a commendable $PM_{1.0}$ removal efficiency of over 91% and maintained a low-pressure drop.[32] Nevertheless, the current obstacle of cost hinders the broad commercialization of this approach. Another trilayer membrane with poly-ϵ-caprolactone/gelatin/ϵ-poly-L-lysine showed biodegradability and 98.82% $PM_{2.5}$ FE. However, it overlooked $PM_{0.3}$ filtration, crucial for addressing pathogen transmission.[34] To tackle these challenges, there is a growing need for a biodegradable face mask that can effectively filter $PM_{0.3}$ particles by using economical materials. One promising solution is the utilization of silk biopolymers, which boast both biodegradability and mechanical strength, making them suitable for capturing $PM_{0.3}$ particles containing pathogens.[35−37] The inherent mechanical and thermal resilience of the silk fibroin protein's β-sheet structure makes it an appealing candidate for developing face masks that can be self-sanitized.[38−41]

Our work has developed an innovative approach by synergistically combining controlled acid hydrolysis and mechanical chopping to create a silk nanofibrous network (SNN). This network is integrated with a stainless steel (SS) mesh, yielding a face mask capable of self-sanitization. Notably, our design demonstrated exceptional FE, achieving 91.4, 95.4, and 98.3% for $PM_{0.3}$, $PM_{0.5}$, and $PM_{1.0}$, respectively, while ensuring comfortable breathability (ΔP = 92 Pa). Additionally, the in situ Joule heating of the SS mesh, achievable with a low actuation voltage, enables the spontaneous inactivation of pathogens such as *Escherichia coli* bacteria within the face mask. Moreover, the natural biodegradation of the SNN in the filter media contributes to its ecofriendliness, facilitating biodegradation in the environment. This innovative work represents a significant advancement, achieving both self-sanitization and biodegradability simultaneously within a face mask filter, a first of its kind.

RESULTS AND DISCUSSION

The self-sanitizable face masks are fabricated by using an SNN and SS mesh. Here, the high-density SNN facilitates efficient filtration of $PM_{0.3}$. The mechanical chopping of degummed silk produces microfibers of dimensions 8 μm, which is unsuitable for capturing $PM_{0.3}$ particles.[42] Conventional acid hydrolysis readily produces silk fibroin solution incompatible with face mask fabrication.[43,44] In this context, we have developed simple acid hydrolysis and mechanical chopping to fabricate the SNN for $PM_{0.3}$ filters. First, *Bombyx mori* cocoons were sliced into fine pieces and degummed to remove the sericin protein for extracting pure silk (see Figure 1a,b).[45] The controlled acid hydrolysis is performed on degummed silk for

https://doi.org/10.1021/acsomega.3c08020
ACS Omega 2024, 9, 9137−9146

30 min to accomplish silk microfibers (Figure 1c). However, a longer duration of acid hydrolysis results in a silk fibroin solution.[44] In the next step, the silk microfibers are mechanically chopped in an aqueous solution to obtain a uniform silk nanofibrous dispersion (see Figure 1d). Here, the unique amalgamation of acid hydrolysis and mechanical chopping is crucial to synthesize SNN. Thus, the obtained silk nanofibrous solution is cast in a Petri dish and dried naturally to obtain nanoporous SNN layers employed as a biodegradable face mask (see Figure 1e,g). In the final step, an SS mesh is incorporated inside the SNN to facilitate in situ self-sanitization in the face mask, as shown in Figure 1e,f.

Here, we chose the commercially available SS mesh for Joule heating, which is rigid and unsuitable for a wearable face mask. More importantly, the low sheet resistance of the pristine SS mesh (1 Ω/sq) requires high actuation currents for Joule heating.[46] Therefore, the pristine SS mesh is etched to decrease the diameter and utilized in the wearable face mask (details in Figure S1, Supporting Information). The SS mesh etching process is inspected by using XRD, as demonstrated in Figure 2a. The SS metal characteristic XRD peaks are intact after the etching process, revealing the robust crystallinity of the SS mesh.[47,48] The structural morphology of the SS mesh is carefully examined with etching time, and the corresponding microwire diameter and pitch, i.e., the distance between two consecutive SS microwires, are depicted in Figure 2b. The

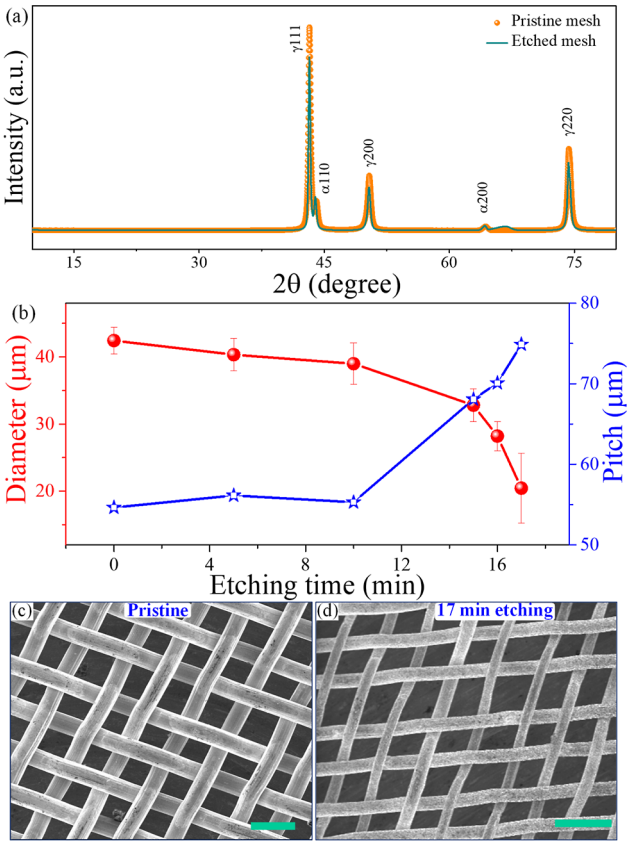

Figure 2. Structural and morphological characterization of the SS mesh: (a) X-ray diffraction (XRD) patterns of the pristine and etched SS mesh and (b) average diameter and pitch of the SS mesh as a function of etching time in acidic solution. FESEM micrographs of the (c) pristine and (d) etched SS mesh, respectively (scale bar, 100 μm each).

representative optical microscope images are presented in the Supporting Information in Figure S2. The SS microwire diameter gradually decreased from 42 to 38 μm for 10 min of etching. However, a sudden decrease in the SS microwire diameter with increased pitch is observed beyond 10 min of etching time. The SS mesh etching time beyond 17 min ruptures the mesh structure, leading to individual microwires, thus, the optimal etching time is 17 min. The average diameters of the wires in the pristine and optimized SS mesh are 42 and 20 μm, respectively (Figure 2c,d). The woven structure of the optimized SS mesh resembles the pristine counterpart, whereas the average pitch in the optimized SS mesh increased to 74 from 54 μm (see Figure 2b). The optimized SS mesh is mechanically flexible and wearable to employ in the face mask, whereas the pristine SS mesh is rigid and inappropriate for wearable devices (Figure S3). Moreover, the optimized SS mesh demonstrated an increased sheet resistance of 6.4 Ω/sq (see Figure S4), which minimizes the requirement of the actuation current for Joule heating.

The optimized SS mesh is sandwiched between SNN layers to fabricate the self-sanitizable face mask. The structural and morphological characterization of self-sanitizable face masks is carried out using XRD and scanning electron microscopy. Figure 3a demonstrates the XRD pattern of the self-sanitizable face mask, which reveals the signature peaks of the SS mesh and pure crystalline silk (inset of Figure 3a).[47−50] The XRD peak at 20.47° (2θ) confirms the formation of silk crystalline β sheets, which instigates mechanical strength and thermal endurance to SNN.[49,50] The optical micrograph of a self-sanitizable face mask (at the boundary) is depicted in Figure 3b, which manifests the existence of the SNN layer and the SS mesh. The inset of Figure 3b shows the optical micrograph of the SNN, which signifies the uniformity of the film over a large area. Moreover, the FESEM images (Figure 3c) disclose entangled SNNs with a high degree of compactness. The magnified view of the silk layer in the inset of Figure 3d exhibits a nanoporous structure composed of a 30−70 nm SNN. The nanoporous structure of silk face masks facilitates the filtration of PM ($PM_{0.3}$) through interception, inertial impaction, Brownian diffusion, and gravitational settling.[19,51] Conversely, the nanopores in silk face masks are essential for directional airflow to overcome dampness and improve comfort for prolonged usage.[34,52] Therefore, the unique design of the SNN enables the realization of a robust and breathable face mask with the ability to filter $PM_{0.3}$ airborne particles.

To elucidate the mechanical characteristics of face masks, stress−strain analyses are conducted on various materials, including the pristine SS mesh (PSS), etched SS mesh (ESS), an SNN, and a hybrid face mask (ESS/SNN), as illustrated in Figure 3d, revealing distinct mechanical behaviors. Young's modulus (Y) in Figure 3e is determined by evaluating the slope of the linear region in the stress−strain curves. Remarkably, the PSS mesh exhibited exceptional toughness, boasting Young's modulus of ∼918 MPa. Conversely, the ESS mesh demonstrated enhanced flexibility at the expense of toughness, yielding Young's modulus of ∼19 MPa. The SNN exhibited mechanical strength (∼5 MPa) comparable to previously reported silk fibroin networks.[53,54] In contrast, the sandwich structure (ESS/SNN) displayed Young's modulus of ∼32 MPa, indicating a synergistic enhancement in mechanical strength. The combination of ESS mesh toughness and SNN stretchability collectively improved the mechanical strength of the sandwich structure.[55] This robust mechanical flexibility

https://doi.org/10.1021/acsomega.3c08020
ACS Omega 2024, 9, 9137−9146

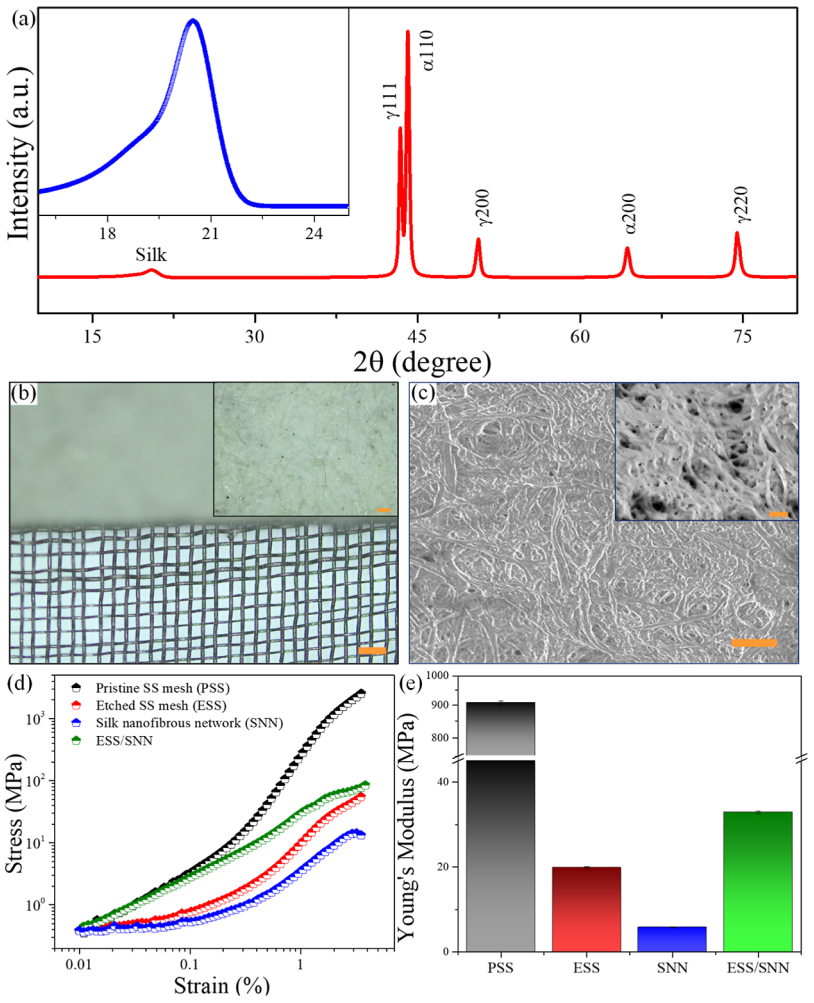

Figure 3. (a) XRD patterns of the SS mesh embedded in the SNN (face mask); inset shows the XRD peak corresponding to the SNN. Optical microscope images of (b) boundary of the SS mesh/SNN; inset SNN (scale bar, 200 and 100 μm, respectively). FESEM images of (c) SNN; inset corresponds to the magnified view (scale bar, 2 μm and 300 nm, respectively). Mechanical properties of the pristine SS mesh (PSS), etched SS mesh (ESS), SNN, and sandwich of the etched SS mesh and SNN (ESS/SNN), (d) representative stress−strain curves, and (e) Young's modulus from the linear region.

validates the practical applicability of the hybrid face mask in real-life scenarios, establishing its suitability for diverse environments.

The self-sanitizable face masks are exposed to PM of size 0.3−1 μm with an indigenously developed PM FE measurement setup, as illustrated in schematic Figure 4a to determine filtering ability. Here, the FE is estimated with the aid of upstream and downstream particles at the interface of the face mask.[56,57] The PM filtration setup consists of the following five main parts: (I) airflow generator, (II) particle generator, (III) particle mixing chamber, (IV) measuring chamber, and (V) particle counter. The airflow generator consisted of a compressor (ELGi TS 05 LD, ELGi Equipment Ltd., Germany) and air filters (Hydint, India). The airflow pressure is maintained at 8 psi using an air pressure regulator. The air filters are employed to eliminate the moisture and dust particles present in the air. A part of the airflow is supplied to the particle generator, where polystyrene latex particles with diameters of 300, 500, and 1000 nm in DI water are aerosolized using a constant output atomizer (TSI 3076, USA). The resultant aerosol is mixed with the second air flow connection (makeup air) from the airflow generator inside a mixing chamber and utilized as an upstream line for FE measurement. The face mask is placed inside the measurement chamber, where it experiences upstream containing aerosolized latex particles. The air flux coming out of the measuring chamber is denoted as a downstream line and connected to a particle counter (TSI particle counter AeroTrak 7110, USA) to measure the downstream particle concentration (C_d). Initially, the upstream line of aerosolized air flow is directly fed to the particle counter to measure the upstream particle concentration (C_u). The FE is estimated using the following eq 1[56]

$$\mathrm{FE} = \frac{C_u - C_d}{C_u} \times 100 \tag{1}$$

The FE setup can measure at variable face velocity from 4.71 to 75 cm/s. The manometer and pressure gauges are connected to upstream and downstream lines, and the particle counter is integrated with a controller and display (SGN Controls, Chandigarh, India). The FE of face masks is measured using the setup mentioned above following the ASTM-Particle Filtration Efficiency standards (F2299). The pressure drop (ΔP) across the face mask is estimated using the following eq 2[56]

$$\Delta P = P_u - P_d \tag{2}$$

https://doi.org/10.1021/acsomega.3c08020
ACS Omega 2024, 9, 9137−9146

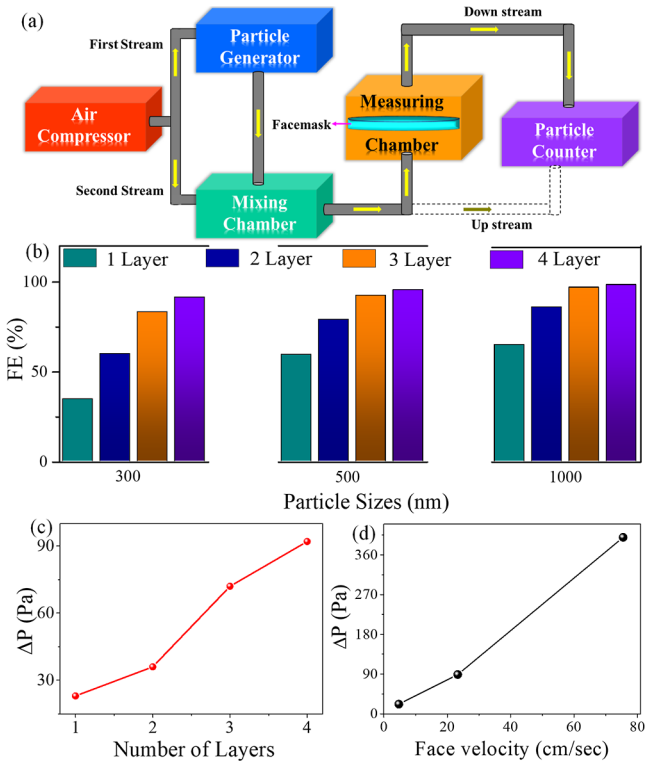

Figure 4. Filtration performance of the SNN-based face masks. (a) Schematic illustration of FE and pressure drop measurement setup. (b) FE of the SNN molded in one layer, two layers, three layers, and four layers for the PM of size 300, 500, and 1000 nm. Differential pressure as a function of (c) SNN layers at a constant face velocity of 4.71 cm/s and (d) face velocity for one layer of the SNN.

where P_d = pressure at the downstream side, and P_u = pressure at the upstream side. It is observed that the FE is gradually increased with the number of free-standing SNN layers irrespective of the PM size (0.3−1 μm; see Figure 4b). The maximum FE is observed for four layers, which are estimated to be 91.4, 95.4, and 98.3% for $PM_{0.3}$, $PM_{0.5}$, and $PM_{1.0}$, respectively. The observed FE of SNN-based face masks is better than synthetic PLLA, PCL/gelatin/ε-PL nanofibrous network.[32,34] However, the low FE for one layer of the SNN is attributed to lower nanopore distribution. The four layers of the SNN exhibited the best filtration efficiencies for all PM. With the increase in layers of the SNN, the face mask captured more PM owing to restricted motion due to a mismatch in porosity.[58] The uniform distribution of the nanopores in SNN over a large surface area facilitates PM filtration and an adequate aerodynamic fluency. In general, the larger PM ($PM_{1.0}$) is captured in face masks due to interception and inertial impaction.[19,51] The smaller PM ($PM_{0.3/0.5}$) is captured in the face mask through the Brownian diffusion mechanism.[19,51] Importantly, the unique design of the face masks with the SNN containing random nanopore distribution demonstrates interception and Brownian diffusion to capture the PM of size 0.3−1 μm. However, increasing the number of layers of the SNN (more than four) in the face mask may improve PM FE at the expense of an increased pressure drop. The diameter of the SNN is crucial for FE, influencing interception and impaction. Smaller diameters provide a larger surface area, enhancing the particle trapping capabilities. Ultrafine SNNs with small nanopores and high porosity effectively capture ultrafine PM, with pore size and distribution influencing particle diffusion and interception by increasing collision probability. Smaller pores improve the capture of

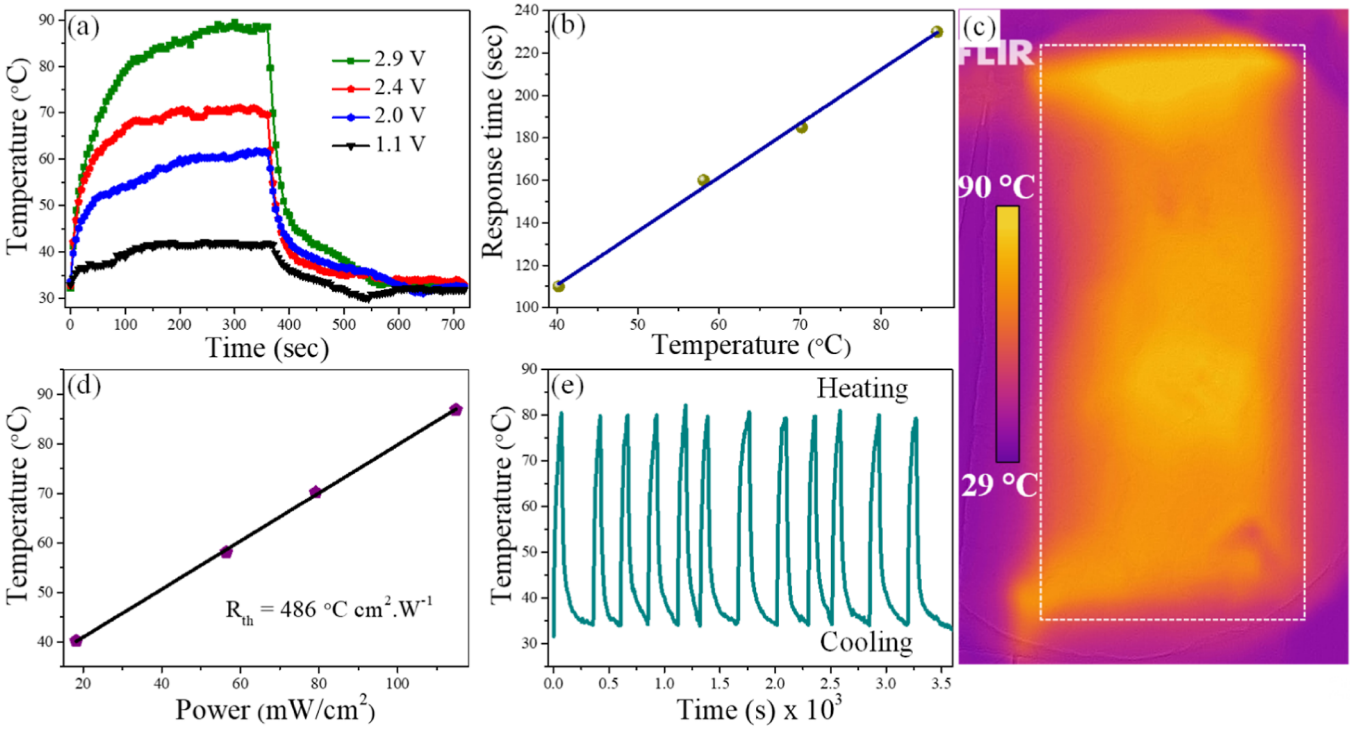

Figure 5. Joule heating performance of a self-sanitizable face mask. (a) Temperature of the face mask as a function of time for the applied bias of 1.1, 2.0, 2.4, and 2.9 V. (b) Response time of the face mask for different saturation temperatures. (c) IR image of the face mask for the applied bias of 2.9 V, scale bar: 1 cm. (d) Saturation temperature vs input power per unit area for the estimation of thermal resistance. (e) Temperature switching cycles of face masks.

https://doi.org/10.1021/acsomega.3c08020
ACS Omega 2024, 9, 9137−9146

smaller particles, and a uniform pore distribution ensures consistent filtration performance across the filter.[59] To optimize nanofiber filter performance, minimizing the airflow resistance is essential, achieved by increasing fiber distance and reducing diameter, as detailed in the study by Kim et al.[60]

The face mask pressure drop must be minimized to increase the breathability and comfort of the wearer. We have estimated the pressure drop by calculating the pressure difference across the face mask.[13,56] As the number of SNN layers increases from 1 to 4, the pressure drop increases from 23 to 92 Pa (Figure 4c). Here, the 4-layer SNN exhibited a small pressure drop of 92 Pa, which is better as compared to (PCL/gelatin/ε-PL, PP-M/PLA-M/PLA-N, PAN, PLA, and spiropyran/polystyrene) reported face masks.[33,34,61,62] We have employed a maximum of four layers of the SNN in face masks to enable breathability for the wearer. The pressure drop of the face mask inevitably depends on the input face velocity. The one layer of the SNN is examined with different face velocities ranging from 4.7 to 75 cm/s, which revealed an increased pressure drop from 23 to 400 Pa (see Figure 4d). Notably, the SNN manifested endurance at 400 Pa pressure, reflecting its mechanical robustness arising from the crystalline β-sheets of silk. Here, the face mask FE is performed at 4.7 cm/s face velocity (28 L/min), similar to the human breathing rate (3.1 cm/s).[63] The SNN-based face mask demonstrated excellent FE, even for small PM ($PM_{0.3}$) with low-pressure drops.

The Joule heating of self-sanitizable face masks is performed with the optimized SS mesh having a sheet resistance of 6.4 Ω/sq. The SS mesh is sandwiched between the SNN as depicted in Figures 1g and 3b. The face masks demonstrated a gradual increase in temperature from 40 to 87 °C when the actuation voltages were increased from 1.1 to 2.9 V, attributed to the local Joule heating of the SS mesh.[64,65] Figure 5a exemplifies a rise in the temperature of the face mask for different actuation voltages as a function of time. A gradual increase in the temperature of the face mask is observed, and a saturation temperature is reached for each actuation voltage. Upon removing the applied bias, the face mask attains room temperature within 400 s. The face masks revealed an increased rise time for higher saturation temperatures, as depicted in Figure 5b.[65] The SS mesh enabled in situ Joule heating of the face mask and consistent heat conduction via the SNN manifested a uniform temperature distribution as depicted in the IR image of Figure 5c.[40,66] The corresponding large-area digital image of the SNN face mask is depicted in Figure S5. The rise in the temperature of the SNN endows disinfection of trapped pathogens inside the face mask. Interestingly, the temperature fall time of the face mask is more than 360 s (Figure 5a), which is a prolonged duration compared to the pristine SS mesh, indicating the seamless heat transfer to the SNN and its ability to sustain the heat. The prolonged fall time supports the effective utilization of heat energy for self-sanitization. The requisite power for Joule heating of the face mask is elucidated with thermal resistance (dT/dP).[65] Figure 5d illustrates a linear dependency of the input power as a function of temperatures of the face mask, employed to determine the thermal resistance and estimated to be 472 °C cm^2 W^{-1}, which is superior as compared to the copper nanowire-based air filter (207 °C cm^2 W^{-1}).[30] The high thermal resistance of the face mask signifies the low power (114 mW/cm^2) requirement for Joule heating and is also reflected in the low actuation voltage (2.9 V). The thermal stability and endurance of the sanitizable face mask are evaluated by switching the temperature from RT to 80 °C, as shown in Figure 5e. The face mask consistently exhibited 12 temperature-switching cycles for an extended duration of 3.5 × 10^3 s. The effect of in situ Joule heating on the thermal stability of the SNN is investigated using thermogravimetric analysis (TGA) and subjecting it to repetitive annealing cycles at 100 °C, as illustrated in Figure S6. These results highlight the thermal stability of the face mask, demonstrating its ability to preserve the structural integrity during disinfection. Therefore, the amalgamation of the SNN and SS mesh in a face mask empowers in situ self-sanitization with low power consumption and efficient distribution of heat. On the other hand, TiO_2 nanofibers decorated with plasmonic Au nanoparticles can degrade PM due to their self-rejuvenating and photocatalytic properties.[67,68] Potential health risks arise if these nanoparticles are inhaled, and their effectiveness is limited without sunlight.[67,68] The self-sanitizable face masks employ in situ Joule heating, which can be activated anytime with an external power supply. Thus, the in situ Joule heating of the face mask facilitates spontaneous disinfection without any chemicals and eventually extends the reusability of the face masks.

The self-sanitizable characteristics of face masks are examined by incubating Gram-negative *E. coli* bacteria on the surface of the SNN.[17] The surface morphology of the cultured *E. coli* bacteria is depicted using FESEM, as shown in Figure 6a,b. The cultured bacteria on the SNN revealed a smooth

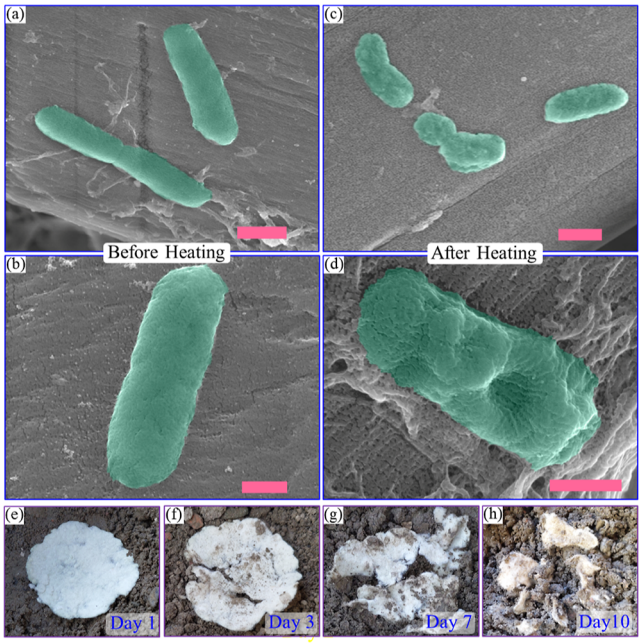

Figure 6. FESEM images of cultured *E. coli* bacteria on the face mask (a,b) before the heat treatment (scale bar: 1 μm and 500 nm, respectively) and (c,d) after the in situ Joule heating at 70 °C for 15 min (scale bar: 1 μm and 500 nm, respectively). Biodegradability test: environmental decomposition of the SNN after exposure to natural soil for (e) 1, (f) 3, (g) 7, and (h) 10 days, respectively.

surface morphology, signifying the existence of healthy and alive *E. coli* bacteria. Furthermore, the face masks are Joule heated with the SS mesh and a portable power supply, instigating a temperature rise. The *E. coli* bacteria is known to inactivate emphatically upon heating at 60 °C. Thus, the Joule heating is performed at 70 °C.[69−71] Interestingly, the requisite actuation voltage for the face mask is only 3 V to maintain a

https://doi.org/10.1021/acsomega.3c08020
ACS Omega 2024, 9, 9137−9146

temperature of 70 °C. After the Joule heating for 15 min, the irregular shape of bacteria and rupturing of the cell surface is observed in the FESEM images of Figure 6c,d. The in situ Joule heating prompts to release water from the bacterial cells, resulting in dehydration and rupturing.[72]

The thermal energy generated during the in situ Joule heating of the face mask dismantles the pathogens captured during PM filtration. The in situ self-sanitization enables spontaneous disinfection to curb the risk of further virus transmission. On the other hand, silk fibers are biodegradable through peptide formation.[35,36] Therefore, the biodegradation of the self-sanitizable face mask is examined in a soil burial as a function of time, as depicted in Figure 6e−h.[32] The SNN demonstrated the instigation of decomposition within 3 days of environmental exposure and manifested disintegration in 10 days.[33] The self-sanitization and the added advantage of biodegradability are challenging to accomplish simultaneously for the first time in face masks (see Table S1, Supporting Information). Moreover, the estimated weight of the hybrid face mask is 6.96 g/m^2, surpassing that of commercially available nonbiodegradable masks while aligning with values of nanofiber-derived face masks (see Table S2, Supporting Information). Therefore, the unique design and development of self-sanitizable and biodegradable face masks enable reusability and open new avenues to combat environmentally lethal microplastic waste.

CONCLUSIONS

We developed a synergistic combination of controlled acid hydrolysis and mechanical chopping to synthesize the SNN, which is amalgamated with the wearable SS mesh to realize self-sanitizable face masks. The unique design of the SNN-based face mask demonstrated an excellent FE of 91.4, 95.4, and 98.3% for $PM_{0.3}$, $PM_{0.5}$, and $PM_{1.0}$, respectively, with comfortable breathability (ΔP = 92 Pa). The uniform distribution of the SNN intrinsically features a dense nanopore distribution and a large surface area, facilitating PM filtration and utmost aerodynamic fluency. The optimized SS mesh in the face mask empowered in situ Joule heating of up to 87 °C with a low actuation voltage of 2.9 V and manifested a superior thermal resistance of 472 °C cm^2 W^{-1}. The in situ Joule heating of the face mask at 70 °C inactivated *E. coli* bacteria situated on the surface of the SNN. The sanitization of face masks is executed without any chemicals or external stimuli, and spontaneous disinfection restrains the risk of further transmission of the virus/pathogens. Moreover, the SNN manifested environmental biodegradation within 10 days. The self-sanitization and added advantage of biodegradability are accomplished simultaneously in a face mask filter for the first time. Therefore, developing self-sanitizable face masks enables spontaneous disinfection and eventually extends their reusability and biodegradability to avoid environmentally lethal microplastic waste.

EXPERIMENTAL SECTION

Materials. The SS mesh (300) with diameter and pitch of 42 and 54 μm, respectively, was purchased from a local vendor. The *B. mori* yellow cocoons were procured from (Aabresham Organic Herbs). Hydrochloric acid (35%) and concentrated sulfuric acid (98%) were purchased from Merck Chemicals, USA, and sodium carbonate was bought from Loba Chemicals, India. Latex particles of sizes 300, 500, and 1000 nm were purchased from Agilent, USA.

Etching of the SS Mesh. The commercially purchased 300 SS mesh was etched using 35 wt % HCl by mixing with distilled water in a 1:2 (v/v) ratio. The acidic solution was heated at 160 °C, and the SS mesh was immersed for 1−20 min. The etching solution was stirred at 500 rpm to maintain a uniform etching throughout the SS mesh. After completing the etching process, the SS mesh was stirred in water for 5 min and subsequently thoroughly washed with water several times. Finally, the ESS mesh was allowed to dry naturally, which was integrated with SNN layers to self-sanitizable face masks.

Synthesis of the SNN for Face Mask Fabrication. The degumming process is illustrated in Figure 1. Initially, the silk cocoons were finely chopped to obtain a size of 3−5 mm, and degumming was performed in 0.02 M sodium carbonate (Na_2CO_3) aqueous solution to remove the sericin protein. The small silk cocoon pieces were added to Na_2CO_3 aqueous solution while maintaining at 120 °C, and the solution was stirred with a glass rod for 2.5 h to dissolve the sericin protein. As a result, the initial transparent solution turns pale yellow. The dispersed silk fibers were recovered and squeezed to remove the excess water. Furthermore, the excess water was removed from the silk fibers by squeezing in between two glass slides. The silk fibers were thoroughly washed with DI water to remove the adsorbed Na_2CO_3. The sericin-free silk fibers were dried overnight under laminar airflow. The approximate yield of the SNN is 0.7−0.8 g for each 1 g of silk cocoons during the degumming process. To synthesize the SNN, the degummed silk fibers were acid hydrolyzed with 30 wt % sulfuric acid while stirring the solution at 500 rpm and maintaining a temperature of 60 °C. A 0.5 g amount of the degummed silk fibers was added to 30 mL of sulfuric acid (30 wt %), and the controlled acid hydrolysis was performed for 30 min. Subsequently, the acidic solution was neutralized by slowly adding DI water. The silk microfibers were subjected to mechanical chopping of 10,000−15,000 rpm using an indigenous setup. The chopping was performed in an aqueous solution until the SNN was obtained. Finally, the SNN solution was cast on a Petri dish with a diameter of 12 cm at a temperature of 60 °C and dried under a laminar flow hood for 24 h. After the completion of drying, a porous and sponge-like SNN-based layer (one layer) was obtained with a thickness of 300 ± 10 μm. The ESS mesh and four layers of SNNs were integrated to fabricate the face mask. During the fabrication of the face mask, the ESS mesh was sandwiched between the four layers of SNNs, where a small amount of DI water was utilized to prompt the adhesion between the SS mesh and the SNN. The total process time of fabricating a self-sanitizable and biodegradable face mask was ∼28 h.

Characterization of the Face Mask. XRD patterns of the SNN and SS mesh were collected using Bruker AXS D8 ADVANCE equipment, USA (40 kV, 40 mA, wavelength ∼0.15406 nm), with Cu Kα radiation. The optical microscope images were captured with an Olympus microscope (BX53M, Japan). The scanning electron microscopy images of the SNN and *E. coli* bacteria were obtained using a ZIESS Sigma 300, Germany. The average diameter and pitch of the SS mesh were analyzed and estimated using ImageJ software. Mechanical performance was carried out in a rheometer with a dynamic mechanical thermal analysis system (model no. MCR 702e Multidrive, Anton Paar Pvt. Ltd.). TGA data were performed with a TGA 4000 PerkinElmer.

https://doi.org/10.1021/acsomega.3c08020
ACS Omega 2024, 9, 9137−9146

Self-Sanitization, Antibacterial, and Biodegradable Experiments. The self-sanitization of the face mask was performed by Joule heating the ESS mesh. The copper foils and wires were soldered at the two ends of the SS mesh of rectangular dimensions of 12 × 5.5 cm^2 for taking the electrical contacts. The copper wires were connected to a portable power supply (HTC Instruments DC 3002-II, India, and cell phone charger) to provide the requisite power (voltage and current) for joule heating. The temperature of the face mask was measured using an infrared sensing camera (FLIR ONE Pro, USA).

The antibacterial experiment was performed with the cultured *E. coli* bacteria on the surface of the face mask. The as-grown *E. coli* bacterial solution 1× phosphate-buffered saline was directly poured on the SNN layer of size 1 × 1 cm^2 placed at the bottom of a 20 mL tube. The incubation process was carried out by pouring the 1 mL of bacterial solution into the SNN layer containing the tube and wrapped with the parafilm for 4 h. After the incubation, the dried SNN layer was transferred to another tube and maintained in a 2.5% glutaraldehyde solution for 30 min. The SNN layer was washed with PBS solution followed by a series of alcohol treatments (20, 40, 60, 80, 90, and 100%). Finally, the SNN layer containing the cultured bacteria was dried and coated with 20 nm of Au before SEM imaging. The self-sanitizable performance of the face mask containing the cultured bacteria was tested by Joule heating the mesh at 70 °C for 15 min. The effect of joule heating on the cultured bacteria was examined by capturing SEM images before and after joule heat treatment. The biodegradability experiment was performed by placing the face mask in a heap of earth inside a natural land field where adequate exposure to air and sunlight was provided. The degradability was observed as a function of the number of days of environmental exposure, and corresponding pictures were captured every 3 days.

■ ASSOCIATED CONTENT

Supporting Information

The Supporting Information is available free of charge at https://pubs.acs.org/doi/10.1021/acsomega.3c08020.

Schematic of SS mesh etching, optical microscope and digital images and sheet resistance of the pristine and etched SS mesh, thermal stability of the SNN, literature comparison, and experimental details (PDF)

■ AUTHOR INFORMATION

Corresponding Author

K. D. M. Rao − *School of Applied & Interdisciplinary Sciences, Indian Association for the Cultivation of Science, Kolkata 700032, India;* orcid.org/0000-0002-5966-3306; Email: saiskdmrao@iacs.res.in, mallik2arjun@gmail.com

Authors

Mozakkar Hossain − *School of Applied & Interdisciplinary Sciences, Indian Association for the Cultivation of Science, Kolkata 700032, India;* orcid.org/0000-0001-5074-2879

Keshab Karmakar − *School of Applied & Interdisciplinary Sciences, Indian Association for the Cultivation of Science, Kolkata 700032, India;* orcid.org/0000-0002-8132-6744

Prakash Sarkar − *School of Applied & Interdisciplinary Sciences, Indian Association for the Cultivation of Science, Kolkata 700032, India;* orcid.org/0000-0002-8930-8452

Tiyasi Chattaraj − *School of Applied & Interdisciplinary Sciences, Indian Association for the Cultivation of Science, Kolkata 700032, India*

Complete contact information is available at: https://pubs.acs.org/10.1021/acsomega.3c08020

Author Contributions

#The manuscript was written through the contributions of all authors. All authors have approved the final version of the manuscript. M.H. and K.K. have contributed equally.

Notes

The authors declare no competing financial interest.

■ ACKNOWLEDGMENTS

M.H. acknowledges UGC for Senior Research fellowship. K.K. acknowledges IACS for the postdoctoral fellowship. P.S. acknowledges UGC for Senior Research fellowship. K.D.M.R. acknowledges the Technical Research Centre (TRC), IACS, Kolkata, and Science and Engineering Research Board (SERB) project CRG/2022/004873 for financial support.

■ REFERENCES

(1) Sahoo, M.; Sethi, N. The Dynamic Impact of Urbanization, Structural Transformation, and Technological Innovation on Ecological Footprint and $PM_{2.5}$: Evidence from Newly Industrialized Countries. *Environ. Dev. Sustain.* **2022**, *24*, 4244−4277.

(2) Wang, S.; Gao, S.; Li, S.; Feng, K. Strategizing the Relation between Urbanization and Air Pollution: Empirical Evidence from Global Countries. *J. Clean. Prod.* **2020**, *243*, 118615.

(3) Ibrahim, M.; Vo, X. V. Exploring the Relationships among Innovation, Financial Sector Development and Environmental Pollution in Selected Industrialized Countries. *J. Environ. Manage.* **2021**, *284*, 112057.

(4) Thangavel, P.; Park, D.; Lee, Y. C. Recent Insights into Particulate Matter ($PM_{2.5}$)-Mediated Toxicity in Humans: An Overview. *Int. J. Environ. Res. Public Health* **2022**, *19*, 7511.

(5) Pryor, J. T.; Cowley, L. O.; Simonds, S. E. The Physiological Effects of Air Pollution: Particulate Matter, Physiology and Disease. *Front. Public Health* **2022**, *10*, 882569.

(6) Ji, X.; Huang, J.; Teng, L.; Li, S.; Li, X.; Cai, W.; Chen, Z.; Lai, Y. Advances in Particulate Matter Filtration: Materials, Performance, and Application. *Green Energy Environ.* **2023**, *8*, 673−697.

(7) Xu, J.; Xiao, X.; Zhang, W.; Xu, R.; Kim, S. C.; Cui, Y.; Howard, T. T.; Wu, E.; Cui, Y. Air-Filtering Masks for Respiratory Protection from $PM_{2.5}$ and Pandemic Pathogens. *One Earth* **2020**, *3*, 574−589.

(8) Vishwakarma, P. K.; Pandey, S. K.; Yadav, S. K.; Shukla, P.; Srivastava, A.; Giri, R. Multiwalled Carbon Nanotube-Based Free-standing Filters for Efficient Removal of Fine Particulate Matters ($PM_{0.3}$), Microplastics ($MP_{0.3}$), and Bioaerosols. *ACS Appl. Nano Mater.* **2022**, *5*, 9306−9318.

(9) Chlebnikovas, A.; Jasevičius, R. Air Pollution with Fine Particles in Closed Parking and Theoretical Studies of the Interaction of Inhaled Particles in Respiratory Tract. *Buildings* **2022**, *12*, 1696.

(10) Shereen, M. A.; Khan, S.; Kazmi, A.; Bashir, N.; Siddique, R. COVID-19 Infection: Emergence, Transmission, and Characteristics of Human Coronaviruses. *J. Adv. Res.* **2020**, *24*, 91−98.

(11) Brooks, J. T.; Butler, J. C. Effectiveness of Mask Wearing to Control Community Spread of SARS-CoV-2. *JAMA* **2021**, *325*, 998−999.

(12) Howard, J.; Huang, A.; Li, Z.; Tufekci, Z.; Zdimal, V.; van der Westhuizen, H. M.; von Delft, A.; Price, A.; Fridman, L.; Tang, L.; Tang, V.; Watson, G. L.; Bax, C. E.; Shaikh, R.; Questier, F.; Hernandez, D.; Chu, L. F.; Ramirez, C. M.; Rimoin, A. W. An

Evidence Review of Face Masks against COVID-19. *Proc. Natl. Acad. Sci. U.S.A.* **2021**, *118*, No. e2014564118.
(13) Zhao, M.; Liao, L.; Xiao, W.; Yu, X.; Wang, H.; Wang, Q.; Lin, Y. L.; Kilinc-balci, F. S.; Price, A.; Chu, L.; Chu, M. C.; Chu, S.; Cui, Y. Household Materials Selection for Homemade Cloth Face Coverings and Their Filtration Efficiency Enhancement with Triboelectric Charging. *Nano Lett.* **2020**, *20*, 5544−5552.
(14) Bandi, M. M. Electrocharged Facepiece Respirator Fabrics Using Common Materials. *Proc. R. Soc. A* **2020**, *476*, 20200469.
(15) Purwar, T.; Esquivel-Puentes, H. A.; Pulletikurthi, V.; Li, X.; Doosttalab, A.; Nelson, C. E.; Appiah, R. E.; Blatchley, E. R.; Castano, V.; Castillo, L. Novel Sustainable Filter for Virus Filtration and Inactivation. *Sci. Rep.* **2022**, *12*, 9109.
(16) Dahanayake, M. H.; Athukorala, S. S.; Jayasundera, A. C. A. Recent Breakthroughs in Nanostructured Antiviral Coating and Filtration Materials: A Brief Review. *RSC Adv.* **2022**, *12*, 16369−16385.
(17) Nguyen, M. C. T.; Nguyen, H. Q.; Jang, H.; Noh, S.; Sohn, Y.; Yee, K.; Jung, H.; Kim, J. Effective Inactivation of Bacillus Atrophaeus Spores and Escherichia Coli on Disposable Face Masks Using Ultraviolet Laser Irradiation. *J. Anal. Sci. Technol.* **2022**, *13*, 23.
(18) Rodriguez-martinez, C. E.; Sossa-Briceño, M. P.; Cortes, J. A. Decontamination and reuse of N95 Filtering Facemask Respirators: A Systematic Review of the Literature. *Am. J. Infect. Control* **2020**, *48*, 1520−1532.
(19) Karmacharya, M.; Kumar, S.; Gulenko, O.; Cho, Y. Advances in Face masks during the COVID-19 Pandemic Era. *ACS Appl. Bio Mater.* **2021**, *4*, 3891−3908.
(20) Lin, N.; Verma, D.; Saini, N.; Arbi, R.; Munir, M.; Jovic, M.; Turak, A. Antiviral Nanoparticles for Sanitizing Surfaces: A Roadmap to Self-Sterilizing against COVID-19. *Nano Today* **2021**, *40*, 101267.
(21) Faridi-Majidi, R.; Norouz, F.; Boroumand, S.; Nasrollah Tabatabaei, S.; Faridi-Majidi, R. Decontamination Assessment of Nanofiber-Based N95 Masks. *Environ. Sci. Pollut. Res.* **2022**, *29*, 80411−80421.
(22) Pascoe, M. J.; Robertson, A.; Crayford, A.; Durand, E.; Steer, J.; Castelli, A.; Wesgate, R.; Evans, S. L.; Porch, A.; Maillard, J. Dry Heat and Microwave-Generated Steam Protocols for the Rapid Decontamination of Respiratory Personal Protective Equipment in Response to COVID-19-Related Shortages. *J. Hosp. Infect.* **2020**, *106*, 10−19.
(23) Kumar, A.; Soni, V.; Singh, P.; Parwaz Khan, A. A.; Nazim, M.; Mohapatra, S.; Saini, V.; Raizada, P.; Hussain, C. M.; Shaban, M.; Marwani, H. M.; Asiri, A. M. Green Aspects of Photocatalysts during Corona Pandemic: A Promising Role for the Deactivation Of COVID-19 virus. *RSC Adv.* **2022**, *12*, 13609−13627.
(24) (a) Ontiveros, C. C.; Sweeney, C. L.; Smith, C.; Macisaac, S.; Bennett, J. L.; Munoz, S.; Stoddart, A. K.; Gagnon, G. A. Assessing the Impact of Multiple Ultraviolet Disinfection Cycles on N95 Filtering Facepiece Respirator Integrity. *Sci. Rep.* **2021**, *11*, 12279. (b) Meng, X.; Peng, X.; Xue, J.; Wei, Y.; Sun, Y.; Dai, Y. A Biomass-Derived, All-Day-Round Solar Evaporation Platform for Harvesting Clean Water from Microplastic Pollution. *J. Mater. Chem. A* **2021**, *9* (17), 11013−11024.
(25) (a) Banerjee, R.; Roy, P.; Das, S.; Paul, M. K. A Hybrid Model Integrating Warm Heat and Ultraviolet Germicidal Irradiation Might Efficiently Disinfect Respirators and Personal Protective Equipment. *Am. J. Infect. Control* **2021**, *49*, 309−318. (b) Meng, X.; Yang, J.; Ramakrishna, S.; Sun, Y.; Dai, Y. Gradient Vertical Channels within Aerogels Based on N-Doped Graphene Meshes toward Efficient and Salt-Resistant Solar Evaporation. *ACS Sustain. Chem. Eng.* **2020**, *8* (12), 4955−4965.
(26) (a) Derraik, J. G. B.; Anderson, W. A.; Connelly, E. A.; Anderson, Y. C. Rapid Review of SARS-CoV-1 and SARS-CoV-2 Viability, Susceptibility to Treatment, and the Disinfection and Reuse of PPE, Particularly Filtering Facepiece Respirators. *Int. J. Environ. Res. Public Health* **2020**, *17*, 6117. (b) Wang, Y.; Xu, W.; Zou, X.; Fu, W.; Meng, X.; Jiang, J.; Zheng, Y.; Ramakrishna, S.; Sun, Y.; Dai, Y. MXene-Decorated Flexible Al2O3/TiO2 Nanofibrous Mats with Self-Adaptive Stress Dispersion towards Multifunctional Desalination. *J. Mater. Chem. A* **2023**, *11* (14), 7422−7431.
(27) Damokhi, A.; Yousefinejad, S.; Fakherpour, A.; Jahangiri, M. Improvement of Performance and Function in Respiratory Protection Equipment Using Nanomaterials. *J. Nanoparticle Res.* **2022**, *24*, 76.
(28) Saminan, S.; Julisafrida, L.; Sakdiah, S.; Idayati, R.; Fajri, N.; Iqhrammullah, M. Nanoparticles-Based Face Masks and Respirators for Preventing COVID-19 Transmission: Breathability Versus Biocidal Activities. *Indian J. Forensic Med. Toxicol.* **2021**, *15*, 4107−4116.
(29) Estevan, C.; Vilanova, E.; Sogorb, M. A. Case Study: Risk Associated to Wearing Silver or Graphene Nanoparticle-Coated Facemasks for Protection against COVID-19. *Arch. Toxicol.* **2022**, *96*, 105−119.
(30) Han, S.; Kim, J.; Lee, Y.; Bang, J.; Kim, C. G.; Choi, J.; Min, J.; Ha, I.; Yoon, Y.; Yun, C.; Cruz, M.; Wiley, B. J.; Ko, S. H. Transparent Air Filters with Active Thermal Sterilization. *Nano Lett.* **2022**, *22*, 524−532.
(31) Xiong, J.; Li, A.; Liu, Y.; Wang, L.; Qin, X.; Yu, J. Multi-Scale Nanoarchitectured Fibrous Networks for High-Performance, Self-Sterilization, and Recyclable Face Masks. *Small* **2022**, *18*, 2105570.
(32) Le, T. T.; Curry, E. J.; Vinikoor, T.; Das, R.; Liu, Y.; Sheets, D.; Tran, K. T. M.; Hawxhurst, C. J.; Stevens, J. F.; Hancock, J. N.; Bilal, O. R.; Shor, L. M.; Nguyen, T. D. Piezoelectric Nanofiber Membrane for Reusable, Stable, and Highly Functional Face Mask Filter with Long-Term Biodegradability. *Adv. Funct. Mater.* **2022**, *32*, 2113040.
(33) Wang, L.; Gao, Y.; Xiong, J.; Shao, W.; Cui, C.; Sun, N.; Zhang, Y.; Chang, S.; Han, P.; Liu, F.; He, J. Biodegradable and High-Performance Multiscale Structured Nanofiber Membrane as Mask Filter Media via Poly (Lactic Acid) Electrospinning. *J. Colloid Interface Sci.* **2022**, *606*, 961−970.
(34) Lan, X.; Wang, H.; Liu, Y.; Chen, X.; Xiong, J.; Mai, R.; Wang, Y.; Cai, N.; Chen, X.; Tang, Y. Biodegradable Trilayered Micro/Nanofibrous Membranes with Efficient Filtration, Directional Moisture Transport and Antibacterial Properties. *Chem. Eng. J.* **2022**, *447*, 137518.
(35) Niu, Q.; Wei, H.; Hsiao, B. S.; Zhang, Y. Biodegradable silk fibroin-based bio-piezoelectric/triboelectric nanogenerators as self-powered electronic devices. *Nano Energy* **2022**, *96*, 107101.
(36) Li, C.; Guo, C.; Fitzpatrick, V.; Ibrahim, A.; Zwierstra, M. J.; Hanna, P.; Lechtig, A.; Nazarian, A.; Lin, S. J.; Kaplan, D. L. Design of Biodegradable, Implantable Devices towards Clinical Translation. *Nat. Rev. Mater.* **2020**, *5*, 61−81.
(37) Zhu, B.; Wang, H.; Leow, W. R.; Cai, Y.; Loh, X. J.; Han, M.; Chen, X. Silk Fibroin for Flexible Electronic Devices. *Adv. Mater.* **2016**, *28*, 4250−4265.
(38) Liang, Y.; Allardyce, B. J.; Kalita, S.; Uddin, M. G.; Shafei, S.; Perera, D.; Remadevi, R. C. N.; Redmond, S. L.; Batchelor, W. J.; Barrow, C. J.; Dilley, R. J.; Schniepp, H. C.; Wang, X.; Rajkhowa, R. Protein Paper from Exfoliated Eri Silk Nanofibers. *Biomacromolecules* **2020**, *21*, 1303−1314.
(39) Zhu, L.; Lin, J.; Pei, L.; Luo, Y.; Li, D.; Huang, Z. Recent Advances in Environmentally Friendly and Green Degumming Processes of Silk for Textile and Non-Textile Applications. *Polymers* **2022**, *14*, 659.
(40) Huang, J.; Xu, Z.; Qiu, W.; Chen, F.; Meng, Z.; Hou, C.; Guo, W.; Liu, X. Y. Stretchable and Heat-Resistant Protein-Based Electronic Skin for Human Thermoregulation. *Adv. Funct. Mater.* **2020**, *30*, 1910547.
(41) Zakrzewska, A.; Haghighat Bayan, M. A.; Nakielski, P.; Petronella, F.; De Sio, L.; Pierini, F. Nanotechnology Transition Roadmap toward Multifunctional Stimuli-Responsive Face Masks. *ACS Appl. Mater. Interfaces* **2022**, *14*, 46123−46144.
(42) Liang, Y.; Allardyce, B. J.; Kalita, S.; Uddin, M. G.; Shafei, S.; Perera, D.; Remadevi, R. C. N.; Redmond, S. L.; Batchelor, W. J.; Barrow, C. J.; Dilley, R. J.; Schniepp, H. C.; Wang, X.; Rajkhowa, R. Correction to "Protein Paper from Exfoliated Eri Silk Nanofi Bers". *Biomacromolecules* **2020**, *21*, 1645.

https://doi.org/10.1021/acsomega.3c08020
ACS Omega 2024, 9, 9137−9146

(43) (a) Kim, H. H.; Kim, J. W.; Choi, J.; Park, Y. H.; Ki, C. S. Characterization of Silk Hydrogel Formed with Hydrolyzed Silk Fi Broin- Methacrylate via Photopolymerization. *Polymer* **2018**, *153*, 232−240. (b) Hu, Y.; Yu, J.; Liu, L.; Fan, Y. Preparation of natural amphoteric silk nanofibers by acid hydrolysis. *J. Mater. Chem. B* **2019**, *7*, 1450−1459.
(44) Lin, M.; Xie, W.; Cheng, X.; Yang, Y.; Sonamuthu, J.; Zhou, Y.; Yang, X.; Cai, Y. Fabrication of silk fibroin film enhanced by acid hydrolyzed silk fibroin nanowhiskers to improve bacterial inhibition and biocompatibility efficacy. *J. Biomater. Sci., Polym. Ed.* **2022**, *33*, 1308−1323.
(45) Rockwood, D. N.; Preda, R. C.; Yücel, T.; Wang, X.; Lovett, M. L.; Kaplan, D. L. Materials Fabrication from Bombyx Mori Silk Fibroin. *Nat. Protoc.* **2011**, *6*, 1612−1631.
(46) Kim, H. J.; Kim, Y. Copper Micromesh-Based Lightweight Transparent Conductor with Short Response Time for Wearable Heaters. *Micro Nano Syst. Lett.* **2021**, *9*, *6*.
(47) Li, B.; Ren, F. C.; Tang, X. Y. The Investigation on Strain Strengthening Induced Martensitic Phase Transformation of Austenitic Stainless Steel: A Fundamental Research for the Quality Evaluation of Strain Strengthened Pressure Vessel. *IOP Conf. Series: Earth Environ. Sci.* **2018**, *128*, 012005.
(48) Hammood, A. S. Biomineralization of 2304 Duplex Stainless Steel with Surface Modification by Electrophoretic Deposition. *J. Appl. Biomater. Funct. Mater.* **2020**, *18*, 228080001989621.
(49) Hu, Y.; Liu, L.; Yu, J.; Wang, Z.; Fan, Y. Preparation of Natural Multicompatible Silk Nanofibers by Green Deep Eutectic Solvent Treatment. *ACS Sustainable Chem. Eng.* **2020**, *8*, 4499−4510.
(50) Kim, H.; Kim, J.; Jun, K.; Kim, J.; Seung, W.; Kwon, O. H.; Park, J.; Kim, S.; Oh, I. Silk Nanofiber-Networked Bio-Triboelectric Generator: Silk Bio-TEG. *Adv. Energy Mater.* **2016**, *6*, 1502329.
(51) Dhanraj, D. I. A.; Choudhary, S.; Jammalamadaka, U.; Ballard, D. H.; Kumfer, B. M.; Dang, A. J.; Williams, B. J.; Meacham, K. W.; Axelbaum, R. L.; Biswas, P. Size-Dependent Filtration Efficiency of Alternative Face mask Filter Materials. *Materials* **2021**, *14*, 1868.
(52) He, R.; Li, J.; Chen, M.; Zhang, S.; Cheng, Y.; Ning, X.; Wang, N. Tailoring Moisture Electroactive Ag/Zn@Cotton Coupled with Electrospun PVDF/PS Nanofibers for Antimicrobial Face Masks. *J. Hazard. Mater.* **2022**, *428*, 128239.
(53) Chan, A. H. P.; Filipe, E. C.; Tan, R. P.; Santos, M.; Yang, N.; Hung, J.; Feng, J.; Nazir, S.; Benn, A. J.; Ng, M. K. C.; Rnjak-Kovacina, J.; Wise, S. G. Altered Processing Enhances the Efficacy of Small-Diameter Silk Fibroin Vascular Grafts. *Sci. Rep.* **2019**, *9*, 17461.
(54) Yang, N.; Moore, M. J.; Michael, P. L.; Santos, M.; Lam, Y. T.; Bao, S.; Ng, M. K. C.; Rnjak-Kovacina, J.; Tan, R. P.; Wise, S. G. Silk Fibroin Scaffold Architecture Regulates Inflammatory Responses and Engraftment of Bone Marrow-Mononuclear Cells. *Adv. Healthcare Mater.* **2021**, *10*, 202100615.
(55) Varanges, V.; Caglar, B.; Lebaupin, Y.; Batt, T.; He, W.; Wang, J.; Rossi, R. M.; Richner, G.; Delaloye, J. R.; Michaud, V. On the Durability of Surgical Masks after Simulated Handling and Wear. *Sci. Rep.* **2022**, *12*, 4938.
(56) (a) Konda, A.; Prakash, A.; Moss, G. A.; Schmoldt, M.; Grant, G. D.; Guha, S. Aerosol Filtration Efficiency of Common Fabrics Used in Respiratory Cloth Masks. *ACS Nano* **2020**, *14*, 6339−6347. (b) Zhao, M.; Liao, L.; Xiao, W.; Yu, X.; Wang, H.; Wang, Q.; Lin, Y. L.; Kilinc-Balci, F. S.; Price, A.; Chu, L.; Chu, M. C.; Chu, S.; Cui, Y. Household Materials Selection for Homemade Cloth Face Coverings and Their Filtration Efficiency Enhancement with Triboelectric Charging. *Nano Lett.* **2020**, *20*, 5544−5552.
(57) Bai, Y.; Han, C. B.; He, C.; Gu, G. Q.; Nie, J. H.; Shao, J. J.; Xiao, T. X.; Deng, C. R.; Wang, Z. L. Washable Multilayer Triboelectric Air Filter for Efficient Particulate Matter $PM_{2.5}$ Removal. *Adv. Funct. Mater.* **2018**, *28*, 1706680.
(58) Talukder, M. E.; Alam, F.; Pervez, M. N.; Jiangming, W.; Hassan, F.; Stylios, G. K.; Naddeo, V.; Song, H. New Generation Washable PES Membrane Face Mask for Virus Filtration. *Nanocomposites* **2022**, *8*, 13−23.
(59) Xue, J.; Wu, T.; Dai, Y.; Xia, Y. Electrospinning and Electrospun Nanofibers: Methods, Materials, and Applications. *Chem. Rev.* **2019**, *119*, 5298−5415.
(60) Kim, S. C.; Kang, S.; Lee, H.; Kwak, D. B.; Ou, Q.; Pei, C.; Pui, D. Y. H. Nanofiber Filter Performance Improvement: Nanofiber Layer Uniformity and Branched Nanofiber. *Aerosol Air Qual. Res.* **2020**, *20*, 80−88.
(61) Xu, Y.; Zhang, X.; Teng, D.; Zhao, T.; Li, Y.; Zeng, Y. Multi-layered micro/nanofibrous non-wovens for functional face mask filter. *Nano Res.* **2022**, *15*, 7549−7558.
(62) Ding, S.; Cao, Y.; Huang, F.; Wang, Y.; Li, J.; Chen, S. Spontaneous Polarization Induced Electrostatic Charge in Washable Electret Composite Fabrics for Reusable Air-Filtering Application. *Compos. Sci. Technol.* **2022**, *217*, 109093.
(63) Rengasamy, S.; Shaffer, R.; Williams, B.; Smit, S. A Comparison of Face mask and Respirator Filtration Test Methods. *J. Occup. Environ. Hyg.* **2017**, *14*, 92−103.
(64) Gupta, R.; Rao, K. D. M.; Kiruthika, S.; Kulkarni, G. U. Visibly Transparent Heaters. *ACS Appl. Mater. Interfaces* **2016**, *8* (20), 12559−12575.
(65) Hossain, M.; Sibin, K. P.; Rao, K. D. M. Angled-Stencil Lithography Based Metal Mesh/$Ti_3C_2T_x$ MXene Hybrid Transparent Electrodes for Low-Power and High-Performance Wearable Thermotherapy. *J. Mater. Chem. C* **2021**, *9*, 6257−6267.
(66) Lv, L.; Han, X.; Wu, X.; Li, C. Peeling and Mesoscale Dissociation of Silk Fibers for Hybridization of Electrothermic Fibrous Composites. *ACS Sustain. Chem. Eng.* **2020**, *8*, 248−255.
(67) Fu, W.; Xu, W.; Yin, K.; Meng, X.; Wen, Y.; Peng, L.; Tang, M.; Sun, L.; Sun, Y.; Dai, Y. Flexible-in-Rigid Polycrystalline Titanium Nanofibers: A Toughening Strategy from a Macro-Scale to a Molecular-Scale. *Mater. Horiz.* **2023**, *10*, 65−74.
(68) Xu, W.; Fu, W.; Meng, X.; Tang, M.; Huang, C.; Sun, Y.; Dai, Y. One Stone Two Birds: A Sinter-Resistant TiO_2 nanofiber-Based Unbroken Mat Enables PM Capture and: In Situ Elimination. *Nanoscale* **2021**, *13*, 20564−20575.
(69) Biswas, S.; Nazmi, A.; Pitesky, M.; Gallardo, R.; Pandey, P. Thermal Inactivation of Escherichia Coli and Salmonella Typhimurium in Poultry Carcass and Litter at Thermophilic Temperatures. *J. Appl. Poult. Res.* **2019**, *28*, 307−317.
(70) Usajewicz, I.; Nalepa, B. Survival of Escherichia Coli O157:H7 in Milk Exposed to High Temperatures and High Pressure. *Food Technol. Biotechnol.* **2006**, *44*, 33−39.
(71) Rana, Y. S.; Eberly, P. M.; Suehr, Q. J.; Hildebrandt, I. M.; Marks, B. P.; Snyder, A. B. Survival of Escherichia Coli O157:H7 during Moderate Temperature Dehydration of Plant-Based Foods. *Foods* **2021**, *10*, 2162.
(72) Hong, Y.; Shi, W.; Wang, H.; Ma, D.; Ren, Y.; Wang, Y.; Li, Q.; Gao, B. Mechanisms of Escherichia Coli Inactivation during Solar-Driven Photothermal Disinfection. *Environ. Sci. Nano* **2022**, *9*, 1000−1010.

https://doi.org/10.1021/acsomega.3c08020
ACS Omega 2024, 9, 9137−9146